Supporting Information

Spadone et al. 10.1073/pnas.1415439112

SI Materials and Methods

Subjects and Stimuli. In total, 21 right-handed (Edinburgh Inventory) healthy young volunteers (age range = 19–29 y old; 14 females) with no previous psychiatric or neurological history participated in the study. All experiments were conducted with the understanding and written consent of each participant according to the Code of Ethics of the World Medical Association and the Institutional Review Board and Ethics Committee at the University of Chieti. Subjects performed a preliminary behavioral session and an fMRI session, including 15 min of resting-state scans followed by ∼45 min of the experimental task.

Stimuli were generated using the MATLAB Psychtoolbox-3 and consisted of two drifting Gabor patches with the following parameters: 2 cycles/degree (deg) spatial frequency, 0.7 deg/s drift rate, and 3° diameter (Fig. 1*A*). The two gratings were presented at opposite symmetrical locations on the horizontal meridian at an eccentricity of 5.5° from central fixation for the whole duration of the experiment. Subjects were instructed to maintain fixation on a central cross while covertly directing attention to one of two patches to detect briefly presented targets. The targets consisted of a brief (150 ms) change of the patch orientation in either the clockwise or anticlockwise direction, and they occurred, on average, every 9 s. The to-be-attended location was indicated by the appearance of a peripheral cue consisting of a 300-ms isoluminant change in the color (pink or cyan) applied to the two patches. The relevant cue color (e.g., pink) to be attended for a whole block of trials was shown at the beginning of each block at fixation and counterbalanced across blocks. After the first cue was presented, the next cue stimulus could appear at either the currently attended grating (stay cue) or the opposite location/grating, indicating that attention had to be shifted (shift cue). A pseudorandom stimulus sequence was designed to obtain short periods of consecutive cues (two, three, or four cues) of the same type (stay or shift), allowing us to investigate connectivity modulations while subjects maintained or shifted attention for several trials in a row. Cues appeared randomly every two, three, or four repetition times (TRs) within a temporal window of ±400 ms centered on the TR. After each cue, either zero, one, or two targets could be presented. The cue correctly predicted the location of the target with 80% probability (valid trials) but did not predict when the target would appear, thus providing no temporal information. In 20% of the trials, the target appeared at the uncued location (invalid trials). Participants were instructed to discriminate orientation changes as fast as possible by pressing a key of a response pad with their right middle or index finger to indicate clockwise or anticlockwise changes, respectively. The difference between performance at the attended vs. unattended location (valid vs. invalid) was a measure of the efficacy of attention selection. Participants completed 12 fMRI runs that were each 3.5 min in duration.

Eye Movement Recordings. The enrollment in the fMRI study was based on a preliminary behavioral session aimed at measuring task performance and monitoring eye position during task execution with an IR eye-tracking system (Iscan etl-400; RK-826 PCI). From this recruitment session, only subjects who showed a significant validity effect on target accuracy (paired two-sample *t* test; $P = 0.05$) and were able to maintain central fixation were included. Eye position was monitored during the 2 s after cue onset with respect to a 100-ms baseline interval measured before each cue onset. Subjects showing eye movements larger than 1° were excluded. Specifically, 11 subjects were ruled out.

To further verify that the selected group of subjects maintained fixation as well during the fMRI experiment, eye movements were recorded using an MRI-compatible IR eye-tracking system (Iscan etl-400; RK-826 PCI). The event-related time courses of eye position time-locked to the presentation of left and right shift and stay cues were extracted during eight consecutive 250-ms time bins (2 s total) after the cue onset. Plots of the event-related time courses of eye position along the horizontal axis for one representative subject and the average across subjects are shown in Fig. S6. Mean values of eye position were 0.01° ± 0.06° (mean ± SD) and −0.03° ± 0.07° for right and left stay cues, respectively, and 0.04° ± 0.07° and −0.07° ± 0.07° for right and left shift cues, respectively (where negative numbers refer to leftward movements). These small values indicate that subjects accurately maintained fixation not only during periods of maintaining attention but also, after the onset of a cue that shifted attention from one location to another.

fMRI Acquisition and Apparatus. Functional T2*-weighted images were collected on a Philips Achieva 3T Scanner using a gradient-echo-planar imaging sequence to measure the BOLD contrast over the whole brain [TR = 1,869 ms; Time of Echo (TE) = 25 ms; 39 slices acquired in ascending interleaved order; voxel size = 3.59 × 3.59 × 3.59 mm; 64 × 64 matrix; and flip angle = 80°]. Structural images were collected using a sagittal M-PRAGE T1-weighted sequence (TR =8.14 ms; TE = 3.7 ms; flip angle = 8°; voxel size = 1 × 1 × 1 mm) and a T2-weighted sequence (TR =3 s; TE = 80 ms; flip angle = 90°; voxel size = 0.958 × 0.958 × 3 mm; 39 slices). Stimuli were presented using a personal computer running MATLAB software (Mathworks), projected onto a screen situated behind the subject's head, and viewed through a mirror located above the subject's head. Subjects wore MRI-compatible earphones and responded using a Lumina LU400 Response Pad (Cedrus Corporation).

fMRI Preprocessing, Statistical Analysis, and ROI Selection. BOLD images were motion-corrected within and between runs, corrected for across-slice timing differences, resampled into 3-mm isotropic voxels, and warped into 711–2C space, a standardized atlas space (1, 2). Preprocessing included a whole-brain normalization correcting for changes in overall image intensity between BOLD runs. The hemodynamic signals during the task period were analyzed with a general linear model (GLM) without a priori assumption of the hemodynamic response shape (3). This model provided an unbiased estimate of the time course for cues and targets generating separate Δ-function regressors for each of seven MR frames after their onset. The GLM included 12 regressors: initial cues (left and right), standard cues (shift left, shift right, stay left, and stay right), targets (valid left, valid right, invalid left, and invalid right), and additional regressors coding for baseline and linear trend in each scan.

The time courses of the evoked responses to cue stimuli were analyzed at the whole-brain level using voxelwise ANOVAs with cue type (stay and shift), cue location (left and right), and time as factors. The voxelwise ANOVAs were corrected for non-independence of time points by adjusting the degrees of freedom and corrected for multiple comparisons using joint *z*-score/cluster size thresholds (4) corresponding to $z = 3.0$ and a cluster size of 13 face contiguous voxels. A peak–search routine was used to extract ROIs 6 mm in radius, with a minimum 12-mm ROI–ROI distance from the cue type by time and cue location by time

(LxT) statistical maps. Each ROI included about 30 voxels on average.

IFC. We conducted three scans (~5 m each), in which the BOLD signal was measured while subjects maintained fixation on a central black cross shown on a gray display. These fixation resting-state scans were followed by 12 scans (3.5 min each) of the experimental task. After standard preprocessing of BOLD images, data were passed through an additional series of specific processing steps for functional connectivity (IFC) (5). First, runs were concatenated, and data were spatially smoothed using a 6-mm FWHM Gaussian blur. Second, several sources of spurious variance were removed by linear regression: (*i*) six parameters obtained by rigid body head motion correction, (*ii*) signal averaged over the whole brain, (*iii*) signal averaged over the lateral ventricles, and (*iv*) signal averaged over a region centered in the white matter (6, 7). The task-evoked response was removed by adding an additional set of regressors to the list of regressors for IFC preprocessing. These regressors corresponded to the design matrix of the GLM. Therefore, the residual dataset minimized the contribution of the transient evoked responses to individual stimuli (cues and targets) and reflected the variance related to the maintenance of the task sets, which were characterized by the constant allocation of visuospatial attention toward one hemifield. Instead of selecting a standard cutoff (i.e., 0.1 Hz) (5, 8), to select the optimal low-pass cutoff frequency, we estimated the range of responding frequencies for this paradigm. The power spectral density (PSD) of the GLM residuals (averaged across subjects) for task and rest periods was calculated using Welch's averaged modified periodogram method with a Hanning window of 32 samples, no overlap, and a frequency resolution of 0.0167 Hz. Then, a two-way ANOVA with frequency and run type (rest and task) as factors was performed on the PSD values averaged across subjects treating ROIs as the random effect. A main effect of frequency was observed ($F_{16,208}$ = 1,145; $P < 0.0001$), and posthoc tests (Duncan) revealed no significant differences in the PSD after 0.167 Hz (Fig. S3), which was selected as the low-pass cutoff frequency (a similar cutoff is given in ref. 9).

Cross-correlation matrices were computed between all of the ROIs previously selected on the basis of the task-evoked activity. For the task dataset, the connectivity between each ROI pair was assessed by computing the Pearson correlation coefficients between all ROIs voxel pairs for each run and averaging across runs. Thus, correlation coefficient r_{XY} between voxels X and Y was computed as

$$r_{XY} = \frac{\sum_{i=1}^{T}(X_i - \overline{X})(Y_i - \overline{Y})}{\sqrt{\sum_{i=1}^{T}(X_i - \overline{X})^2}\sqrt{\sum_{i=1}^{T}(Y_i - \overline{Y})^2}},$$

where T was the total number of observation, and over bars indicate the overall mean.

Then, the Fisher z transform $z = 1/2\ln[(1+r)/(1-r)]$ was applied. The same procedure was repeated for the resting-state dataset using the same window length as for the task runs and overlapping windows to obtain the same number of averages. Cross-correlation matrices for individual ROI pairs during rest and task execution were obtained by averaging correlation values of all subjects and voxels within that ROI pair (Fig. 2 *A* and *B*). Eventually, we examined task-induced modulations of IFC by computing the difference between task and rest IFC matrices (Fig. 2*C*).

These matrices were submitted to a series of analyses.

i) We evaluated network segregation during rest and task through a two-way ANOVA with condition (rest and task) and network (within DAN, within VIS, and between DAN–VIS) as factors. This analysis was run on the average across pairs of the z Fisher correlation within the submatrices comprising DAN, VIS, and between DAN–VIS (Fig. 2*D*).

ii) We examined whether task execution induced a change in the topology of the within-network correlation patterns by comparing the individual cross-correlation submatrices at rest with task using the Mantel test, which is a statistical test on the correlation between two matrices. The significance of the observed correlation was obtained through comparison with a distribution of values obtained from 10,000 permutations of one of the original matrices.

iii) We directly compared the rest and task connectivity values for each ROI pair by means of paired two-sample t tests (P = 0.05, Bonferroni corrected) with subject as a random effect (*SI Results* discusses single ROI pair comparisons).

iv) We assessed whether task execution induced a network reorganization (and the statistical significance of these topology changes) using an approach based on graph theory. In particular, we first converted the individual correlation matrices at rest and during task into graphs and then, applied the Network-Based Statistics toolbox (10) to test for significant changes in graph components. Network-Based Statistics were used with primary (t statistic) thresholds of 3.0, and each resulting component satisfied a $P < 0.01$ level of significance (Fig. 2*E*).

v) We compared graph modularity across conditions using the Brain Connectivity Toolbox (11). For each subject and condition, modularity was estimated as the mean value obtained from 10,000 runs using the Louvain modularity. The estimated values (for both rest and task) were compared with the associated random graph (mean modularity from 10,000 trials). A t test was used to assess significant changes across conditions.

Finally, we examined the IFC modulations by conducting a nonstationary connectivity analysis. In particular, we obtained functional connectivity matrices corresponding to periods of continuous stay and shift cues according to the following procedure: for each voxel pair comprised in an ROI pair, we computed the time course of the nonstationary correlation using a 16.8-s (nine TRs) sliding window. The correlation at successive increments of one TR was assessed as

$$r_{XY}(t) = \frac{\sum_{i=t}^{t+9}(X_i - \overline{X})(Y_i - \overline{Y})}{\sqrt{\sum_{i=t}^{t+9}(X_i - \overline{X})^2}\sqrt{\sum_{i=t}^{t+9}(Y_i - \overline{Y})^2}},$$

where over bars indicate the mean over the appropriate window. The matrices representing the stay- and shift-specific IFCs were produced by averaging over the voxel pairs within each ROI pair and over time the nonstationary correlation during periods of consecutive stay and shift cues. These periods, randomly included in the experiment, were about 40 for each attentional condition (stay and shift) and characterized by an average length of 8.6 TRs. To consider the intrinsic spread of the nonstationary time course, the last four points (one-half window) of each period were excluded from the average. Then, a Fisher z transform was applied to the average nonstationary correlation, and the values of connectivity during resting state were subtracted.

To assess the functional significance of task-induced modulations of IFC, we calculated the correlation between IFC modulations (task-, shift-, and stay-specific) and behavioral performance (discrimination accuracy in valid conditions) across subjects using Pearson tests. This analysis was performed on both submatrices (P = 0.05, FDR corrected) and ROI correlation matrices (P = 0.05) (Fig. 3*A* and Fig. S5). When the correlation between behavior and IFC was examined at the level of the different ROI pairs, the results did not survive the correction for multiple

comparisons because of the large number of comparisons. The analysis was restricted to submatrices showing a significant task-induced modulation of the IFC and to the ROIs comprised in these submatrices. Examples of this IFC–behavior correlation are shown in Fig. 3 *B* and *C* for L-dFEF vs. L-V3a–V7 and R-MT vs. L-V3a–V7, respectively.

DFC. Directional connectivity was studied by Granger Causality (GC) analysis using the MATLAB Toolbox Granger Causal Connectivity Analysis (12). This method estimates the influence of signal X in predicting signal Y (unrestricted model) compared with the prediction offered by the past of signal Y itself (restricted model) (13). The approach has been successfully applied to fMRI time series (14) and more specifically, in the context of visuospatial attention by Bressler et al. (15). It has to be noted, however, that the GC method faces methodological challenges associated with the effect of sampling rate and the different lags of hemodynamic responses across areas (16, 17). Recent work indicates that it is possible to use GC analyses to fMRI by applying strategies of analyses that minimize the above issues (14, 18, 19). For instance, our analysis focuses on GC changes between two conditions, which is a more conservative approach with respect to the analyses of single conditions given sampling rate limitation and heterogeneity of neurovascular coupling across regions (18).

The amount of causality from X to Y was assessed by considering two regression models: (i) the restricted model $Y(t) = \alpha_1 Y(t-m) + \varepsilon_1(t)$ and (ii) the unrestricted model $Y(t) = \alpha_2 Y(t-m) + \beta X(t-m) + \varepsilon_2(t)$, where $Y(t)$ is the Y time series at time t; $Y(t-m)$ is the m-lagged Y time series; α_1, α_2, and β are the regression coefficients, and ε_1 and ε_2 are the model residuals. Reduction of variability of the unrestricted model residual quantified causal influence. It was measured as an F statistic that approximately follows an F distribution with degrees of freedom m and $T - 2m - 1$:

$$F = \frac{\frac{RSS_r - RSS_{ur}}{m}}{\frac{RSS_{ur}}{T-2m-1}},$$

where RSS_r is the restricted residual sum of squares, RSS_{ur} is the unrestricted residual sum of squares, m is the model order (the number of lagged observations to include in the regression model), and T is the total number of observations. The F statistic was significant when it was larger than the critical value at $P < 0.05$ in the standard $F_{m,T-2m-1}$. To estimate GC, we adopted bivariate autoregressive models of order 2 between BOLD residuals of each pairwise combination of voxels. The best model order was selected using the Bayesian information criterion. In addition, we verified that the residuals of the models were uncorrelated using the Durbin–Watson test (20) and that the portion of the data captured by the models was greater than 80% using the consistency test (21). Both conditions were satisfied for all subjects. Computing a separate bivariate autoregressive model for each voxel pair avoids the possible pitfalls of across-voxel averages and is more stable than multivariate model because of the large dimensionality of observations. However, we acknowledge that this approach is not taking into account possible effects of other driving or intermediate time series (22). Maps were produced by computing F statistics for any two ROIs in both directions between residuals of every voxel pair in those ROIs and computing the fractions of F statistics that were significant (Granger consistency) (15). The consistencies of all ROI pairs were shown in a matrix in which rows were the sources either at rest (Fig. 4*A*) and during task execution (Fig. 4*B*). Then, the difference between task and rest consistencies was computed (Fig. 4*C*), and a group statistical analysis of directional connectivity changes was performed on the differences between task and rest consistency values from the individual subjects. In particular, a paired two-sample t test with subject as a random effect was conducted with a significance threshold of $P = 0.05$ (FDR corrected). In Fig. S3, a flowchart of the described procedure is shown.

SI Results

Pairwise Difference Between Task and Rest IFC Matrices (Single ROI Pair Comparisons). A direct test of the difference between rest and task conditions revealed a significant modulation within the VIS and between the VIS and the DAN but not within the DAN (Fig. 2*C*). Interestingly, we observed a decrease of correlation between visual regions that was particularly evident in homotopic ROIs (e.g., left and right V3a–V7). In contrast, we observed an increase of IFC between several regions of the DAN, including dFEF and R-SPL, and all regions of the VIS independently of hemisphere. A between-network increase of IFC was also observed between the VIS and the other parietal regions (PreCu and vTPJ).

Control Analysis on Visuotopic ROIs. To control that the observed general decrease of correlation within VIS regions (MT, V3a–V7, and V4–V8) during the attention task did not hide specific increases of correlation between visual regions that have a retinotopic organization, we selected a new set of ROIs including early visual regions, such as V1v, V2v, VP (ventral posterior area), V1d, V2d, and V3. These regions were selected based on the intersection between visuotopic regions from the CARET software (23) (Fig. S4 *A* and *B*) and voxels exhibiting a main effect of time in our experiment (obtained from the voxelwise ANOVA with cue type, cue location, and time as factors) (Fig. S4 *C* and *D*). We used the main effect of time compared with the LxT interaction effect to include enough voxels in early visual cortex (V1 and V2). As for the original ROI set, rest- and task-related cross-correlation matrices were estimated for each ROI pair, and task-induced modulations were computed on the task vs. rest difference. As shown in Fig. S4*E*, the results were qualitatively similar to those observed in our original VIS regions, with a general decrease of the inter- and intrahemispheric IFCs, which particularly involved V3, V3a, V4v, V7, VP, and V8 regions, and no specific increase of IFC between retinotopically correspondent subregions. To quantify this impression, a three-way ANOVA was conducted with task condition (rest and task), correspondence [correspondent (dorsal–dorsal or ventral–ventral) and noncorrespondent (dorsal–ventral ROIs)], and hemispheric relationship [ipsilateral (left–left or right–right) and contralateral (left–right ROIs)] as factors on IFC between V1, V2, and V3/VP early visual regions (Fig. S4*F*). The results indicated a main effect of task ($F_{1,20} = 7.3$; $P = 0.01$), correspondence ($F_{1,20} = 207.8$; $P < 1 \times 10^{-6}$), and hemispheric relationship ($F_{1,20} = 74.4$; $P < 0.1 \times 10^{-6}$) and a significant correspondence by hemispheric relationship interaction ($F_{1,20} = 4.7$; $P < 0.05$) but no significant task condition by correspondence ($F_{1,20} = 1.2$; $P =$ n.s.) or task condition by hemispheric relationship ($F_{1,20} = 0.05$; $P =$ n.s.) and no significant three-way interaction. In summary, we found stronger IFC between retinotopically correspondent regions (e.g., within the left ventral visual cortex V1v, left V2v, and left VP), which is in line with previous studies (24), but also, an overall significant decrease of IFC during attention, with no significant interaction between task condition and other factors. This control analysis generalizes our original findings by excluding the hypothesis that adjacent early visual regions (V1–V3/VP) show specific IFC increases when shifting from rest to attention.

Analysis on DAN ROIs Extracted from Cue LxT Map. Based on previous studies (25–29) on the functional segregation in parietal cortex between shift-related and spatially selective signals (in medial and lateral parietal regions, respectively), a second analysis investigated task-induced modulations of IFC within spatially selective DAN regions that survived the contrast used for defining the VIS network (i.e., cue LxT) and between these regions and the original shift-related DAN regions (i.e., selected from the contrast cue type by time). As shown in Fig. S2*A*, the cue LxT ANOVA interaction indicated a significant contralateral bias in lateral DAN regions of the left but not the right hemisphere (L-dFEF and pIPS; regions labeled as DAN LxT) (signal time courses in Fig. S2 *B* and *C*). This asymmetry is consistent with previous studies showing that contralateral bias for spatial attention is stronger in left dorsal visual areas (30, 31). To examine the behavior of these spatially selective DAN regions (DAN LxT) vis à vis previously examined DAN and VIS regions, we measured task-induced IFC and DFC modulations (DAN LxT ROIs are displayed in the last two rows of Fig. S2 *D* and *E*). These spatially selective regions in the DAN show a task-induced increase of IFC ($P < 5 \times 10^{-5}$) as well as stronger IFC with the original DAN regions ($P < 5 \times 10^{-4}$). No significant IFC modulations were observed with VIS regions (P = n.s.). These comparisons were carried out with two-sample t tests between rest and task conditions (Fig. S2*D*). This pattern contrasts with that shown by the original shift-related DAN ROIs, which showed an increased task-induced IFC with VIS regions and no significant within-network modulations. In addition, L-FEF-LxT and L-IPS-LxT showed an increase of DFC both toward our original DAN regions and toward VIS regions.

The observed IFC modulations are consistent with the idea that spatially selective regions of the DAN show a connectivity profile that is intermediate between that of the shift-related DAN regions and that of the spatially selective VIS regions.

SI Discussion

DAN Interaction with Sensory Areas. This study examines for the first time, to our knowledge, the simultaneous modulations of IFC and DFC induced by a visuospatial attention task, with several implications for our understanding of the relationship between the DAN and sensory regions. A key result is that the control of the locus of attention triggers a consistent increase of both measures (IFC and DFC) of DAN–VIS interaction compared with the divergent pattern observed in within-network connectivity. Importantly, the variation of between-network IFC is correlated with target discrimination accuracy.

A relevant question that it is still highly debated in current literature on visuospatial attention is whether the deployment of top-down attention is initiated and controlled by frontal (32, 33) or parietal regions (34, 35). Here, we found that dFEFs played a leading role in the simultaneous IFC/DFC modulation. First, bilateral dFEFs exhibited a strong increase of task-induced IFC with most of the VIS regions (Fig. 2*C*). Second, the association between cross-network IFC and task performance almost inevitably involved left dFEF (Fig. 3). dFEF showed strong directional influence on not only visual but also, parietal cortex (Fig. 4*C*). Therefore, albeit that visual regions received top-down signals from both frontal and parietal cortex, frontal regions also exerted control over multiple parietal sites, supporting a central role of frontal regions in both a serial (frontal > parietal > sensory) and parallel machinery for top-down attention.

During the task and especially, during attentional shifting, the leading receiver counterparts of directed influence from the DAN were the V3a–V7 regions. These regions have been shown to contain a retinotopic map of the space (36), and a study adopting a similar, although widely spaced, paradigm has shown that attention-related signals in V3a–V7 correlate trial by trial with discrimination accuracy (37). In addition, transient inactivation of V3a–V7 regions by transcranial magnetic stimulation has been shown to produce a pattern of contralateral visual impairment (28), consistent with a role in spatial coding and discrimination.

Importantly, our findings also inform the current debate on hemispheric asymmetries of mechanisms for the control of spatial attention (38–40). In particular, a hemispheric asymmetry is suggested by the pattern of between-network DFC shown in Fig. 4*C* (i.e., from the DAN to left visual regions). However, when these hemispheric asymmetries were directly tested through a four-way ANOVA on task-induced DFC from dFEF and SPL to visual regions with visual (MT, V3a–V7, and V4–V8), DAN region (dFEF and SPL), hemispheric relationship (ipsilateral and contralateral), and hemisphere (left and right) as factors, no significant main effect of DAN region ($F_{1,20} = 0.3$; P = n.s.), hemispheric relationship ($F_{1,20} = 0.2$; P = n.s.), and hemisphere ($F_{1,20} = 0.05$; P = n.s.) was found, and no significant interactions were found. Interestingly, the ANOVA only revealed a significant main effect of visual region ($F_{2,40} = 5.28$; $P < 0.01$), explained by a greater directionality from bilateral dFEF and SPL to regions located at the intermediate level of the visual hierarchy (V3a–V7). Although a significant increase of DFC was only detectable toward the left hemisphere VIS regions, the lack of a main effect of hemispheric relationship and any interaction in the ANOVA indicated the absence of any hemispheric asymmetry or contralateral bias. Therefore, these results do not provide support for lateralization of the DAN–VIS interaction.

These findings also provide crucial insights on the role of the DAN and the ventral attention network in the reorienting of spatial attention. In particular, although both networks are thought to participate in reorienting (41), it is still largely unclear which of the two is responsible for the initiation of the reorienting response (41). In particular, despite our task requiring frequent reorienting responses, we did not find any significant evidence of a directional influence of right vTPJ on regions of the DAN or VIS network, and although the study design did not allow to directly examine selective increases of DFC from vTPJ to DAN regions during shifts of attention, the results do not support the idea that the reorienting response is initiated in the temporoparietal junction.

From Rest to Attention: Changes in Connectivity in DAN and VIS Network. Our findings are consistent with a handful of other studies showing a dynamic alteration of resting connectivity during task execution in different domains (42–45). Jointly, these papers provide strong evidence for a qualitatively different functional organization between rest and task states. These findings also suggest that attention selection operates at multiple temporal scales: not only through transient changes in task-evoked modulation (46, 47) or directional influence on visual responses (15, 48, 49) but also, through longer time scales adjustments of functional connectivity. The time scales of BOLD fluctuations and of the related functional connectivity modulations are in the order of tens of seconds. Therefore, in addition to trial to trial modulations, with which the field has been mainly concerned, attention selection sets up preferential connections/interactions over prolonged periods of time across multiple trials.

Notably, works using dynamic causal modeling or psychophysiological interaction (50) typically focus on task-evoked modulations of effective connectivity by using a model of coupling that allows inferences on how directed effective connectivity is affected by experimental factors. Therefore, it would be interesting to revisit our data using these approaches. In addition, because we were explicitly interested in task-induced modulations of patterns of internal segregation/external integration characterizing two RSNs, it would be also interesting to investigate whether a third region (e.g., the thalamus) (51) may control the task-dependent interaction between the two networks.

1. Talairach J, Tournoux P (1988) *Co-Planar Stereotaxic Atlas of the Human Brain: 3-Dimensional Proportional System—An Approach to Cerebral Imaging* (Thieme Medical Publishers, New York).
2. Van Essen DC (2005) A population-average, landmark- and surface-based (PALS) atlas of human cerebral cortex. *Neuroimage* 28(3):635–662.
3. Ollinger JM, Shulman GL, Corbetta M (2001) Separating processes within a trial in event-related functional MRI. *Neuroimage* 13(1):210–217.
4. Forman SD, et al. (1995) Improved assessment of significant activation in functional magnetic resonance imaging (fMRI): Use of a cluster-size threshold. *Magn Reson Med* 33(5):636–647.
5. Fox MD, et al. (2005) The human brain is intrinsically organized into dynamic, anti-correlated functional networks. *Proc Natl Acad Sci USA* 102(27):9673–9678.
6. Fox MD, Corbetta M, Snyder AZ, Vincent JL, Raichle ME (2006) Spontaneous neuronal activity distinguishes human dorsal and ventral attention systems. *Proc Natl Acad Sci USA* 103(26):10046–10051.
7. He BJ, et al. (2007) Breakdown of functional connectivity in frontoparietal networks underlies behavioral deficits in spatial neglect. *Neuron* 53(6):905–918.
8. Biswal B, Yetkin FZ, Haughton VM, Hyde JS (1995) Functional connectivity in the motor cortex of resting human brain using echo-planar MRI. *Magn Reson Med* 34(4): 537–541.
9. Norman-Haignere SV, McCarthy G, Chun MM, Turk-Browne NB (2012) Category-selective background connectivity in ventral visual cortex. *Cereb Cortex* 22(2):391–402.
10. Zalesky A, Fornito A, Bullmore ET (2010) Network-based statistic: Identifying differences in brain networks. *Neuroimage* 53(4):1197–1207.
11. Rubinov M, Sporns O (2010) Complex network measures of brain connectivity: Uses and interpretations. *Neuroimage* 52(3):1059–1069.
12. Seth AK (2010) A MATLAB toolbox for Granger causal connectivity analysis. *J Neurosci Methods* 186(2):262–273.
13. Granger CWJ (1969) Investigating causal relations by econometric models and cross-spectral methods. *Econometrica* 37(3):424–438.
14. Roebroeck A, Formisano E, Goebel R (2005) Mapping directed influence over the brain using Granger causality and fMRI. *Neuroimage* 25(1):230–242.
15. Bressler SL, Tang W, Sylvester CM, Shulman GL, Corbetta M (2008) Top-down control of human visual cortex by frontal and parietal cortex in anticipatory visual spatial attention. *J Neurosci* 28(40):10056–10061.
16. Smith SM, et al. (2011) Network modelling methods for FMRI. *Neuroimage* 54(2): 875–891.
17. Friston K, Moran R, Seth AK (2013) Analysing connectivity with Granger causality and dynamic causal modelling. *Curr Opin Neurobiol* 23(2):172–178.
18. Barnett L, Seth AK (2014) The MVGC multivariate Granger causality toolbox: A new approach to Granger-causal inference. *J Neurosci Methods* 223:50–68.
19. Wen X, Yao L, Liu Y, Ding M (2012) Causal interactions in attention networks predict behavioral performance. *J Neurosci* 32(4):1284–1292.
20. Durbin J, Watson GS (1950) Testing for serial correlation in least squares regression. I. *Biometrika* 37(3-4):409–428.
21. Ding M, Bressler SL, Yang W, Liang H (2000) Short-window spectral analysis of cortical event-related potentials by adaptive multivariate autoregressive modeling: Data preprocessing, model validation, and variability assessment. *Biol Cybern* 83(1):35–45.
22. Tang W, Bressler SL, Sylvester CM, Shulman GL, Corbetta M (2012) Measuring Granger causality between cortical regions from voxelwise fMRI BOLD signals with LASSO. *PLOS Comput Biol* 8(5):e1002513.
23. Van Essen DC (2012) Cortical cartography and Caret software. *Neuroimage* 62(2):757–764.
24. Arcaro MJ, Honey CJ, Mruczek RE, Kastner S, Hasson U (2015) Widespread correlation patterns of fMRI signal across visual cortex reflect eccentricity organization. *eLife* 4:4.
25. Yantis S, et al. (2002) Transient neural activity in human parietal cortex during spatial attention shifts. *Nat Neurosci* 5(10):995–1002.
26. Shulman GL, et al. (2009) Interaction of stimulus-driven reorienting and expectation in ventral and dorsal frontoparietal and basal ganglia-cortical networks. *J Neurosci* 29(14):4392–4407.
27. Capotosto P, et al. (2015) Dynamics of EEG rhythms support distinct visual selection mechanisms in parietal cortex: A simultaneous transcranial magnetic stimulation and EEG study. *J Neurosci* 35(2):721–730.
28. Capotosto P, et al. (2013) Anatomical segregation of visual selection mechanisms in human parietal cortex. *J Neurosci* 33(14):6225–6229.
29. Tosoni A, Shulman GL, Pope AL, McAvoy MP, Corbetta M (2013) Distinct representations for shifts of spatial attention and changes of reward contingencies in the human brain. *Cortex* 49(6):1733–1749.
30. Szczepanski SM, Konen CS, Kastner S (2010) Mechanisms of spatial attention control in frontal and parietal cortex. *J Neurosci* 30(1):148–160.
31. Corbetta M, Kincade JM, Shulman GL (2002) Neural systems for visual orienting and their relationships to spatial working memory. *J Cogn Neurosci* 14(3):508–523.
32. Buschman TJ, Miller EK (2007) Top-down versus bottom-up control of attention in the prefrontal and posterior parietal cortices. *Science* 315(5820):1860–1862.
33. Grent-'t-Jong T, Woldorff MG (2007) Timing and sequence of brain activity in top-down control of visual-spatial attention. *PLoS Biol* 5(1):e12.
34. Green JJ, McDonald JJ (2008) Electrical neuroimaging reveals timing of attentional control activity in human brain. *PLoS Biol* 6(4):e81.
35. Hopf JM, Mangun GR (2000) Shifting visual attention in space: An electrophysiological analysis using high spatial resolution mapping. *Clin Neurophysiol* 111(7):1241–1257.
36. Silver MA, Kastner S (2009) Topographic maps in human frontal and parietal cortex. *Trends Cogn Sci* 13(11):488–495.
37. Sylvester CM, Shulman GL, Jack AI, Corbetta M (2007) Asymmetry of anticipatory activity in visual cortex predicts the locus of attention and perception. *J Neurosci* 27(52):14424–14433.
38. Duecker F, Formisano E, Sack AT (2013) Hemispheric differences in the voluntary control of spatial attention: Direct evidence for a right-hemispheric dominance within frontal cortex. *J Cogn Neurosci* 25(8):1332–1342.
39. Nobre AC, et al. (1997) Functional localization of the system for visuospatial attention using positron emission tomography. *Brain* 120(Pt 3):515–533.
40. Gitelman DR, et al. (1999) A large-scale distributed network for covert spatial attention: Further anatomical delineation based on stringent behavioural and cognitive controls. *Brain* 122(Pt 6):1093–1106.
41. Corbetta M, Patel G, Shulman GL (2008) The reorienting system of the human brain: From environment to theory of mind. *Neuron* 58(3):306–324.
42. Cole MW, Bassett DS, Power JD, Braver TS, Petersen SE (2014) Intrinsic and task-evoked network architectures of the human brain. *Neuron* 83(1):238–251.
43. Gao W, Gilmore JH, Alcauter S, Lin W (2013) The dynamic reorganization of the default-mode network during a visual classification task. *Front Syst Neurosci* 7:34.
44. Fornito A, Harrison BJ, Zalesky A, Simons JS (2012) Competitive and cooperative dynamics of large-scale brain functional networks supporting recollection. *Proc Natl Acad Sci USA* 109(31):12788–12793.
45. Al-Aidroos N, Said CP, Turk-Browne NB (2012) Top-down attention switches coupling between low-level and high-level areas of human visual cortex. *Proc Natl Acad Sci USA* 109(36):14675–14680.
46. Corbetta M, Shulman GL (2002) Control of goal-directed and stimulus-driven attention in the brain. *Nat Rev Neurosci* 3(3):201–215.
47. Kastner S, De Weerd P, Desimone R, Ungerleider LG (1998) Mechanisms of directed attention in the human extrastriate cortex as revealed by functional MRI. *Science* 282(5386):108–111.
48. Ruff CC, et al. (2006) Concurrent TMS-fMRI and psychophysics reveal frontal influences on human retinotopic visual cortex. *Curr Biol* 16(15):1479–1488.
49. Moore T, Armstrong KM (2003) Selective gating of visual signals by microstimulation of frontal cortex. *Nature* 421(6921):370–373.
50. Friston KJ, Harrison L, Penny W (2003) Dynamic causal modelling. *Neuroimage* 19(4): 1273–1302.
51. Saalmann YB, Pinsk MA, Wang L, Li X, Kastner S (2012) The pulvinar regulates information transmission between cortical areas based on attention demands. *Science* 337(6095):753–756.

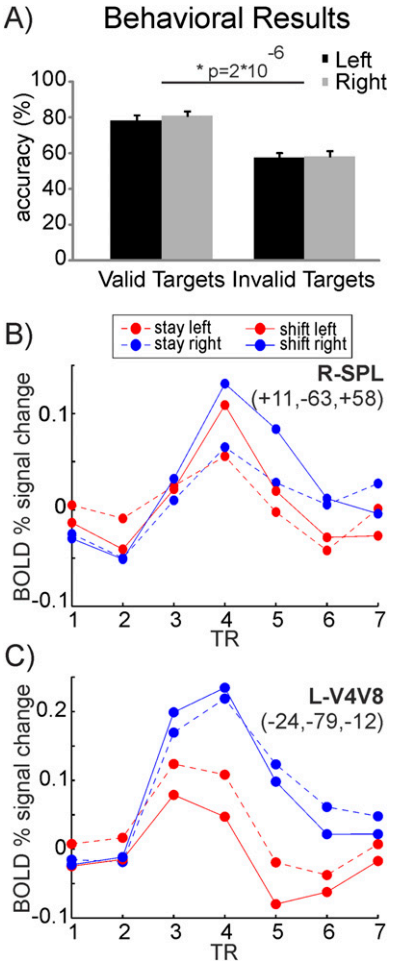

Fig. S1. (*A*) Discrimination accuracy as a function of target location and target validity shows the behavioral advantage of covert spatial attention. (*B* and *C*) For one representative region of each map of ANOVA interaction, time courses of the evoked responses to cue stimuli are shown.

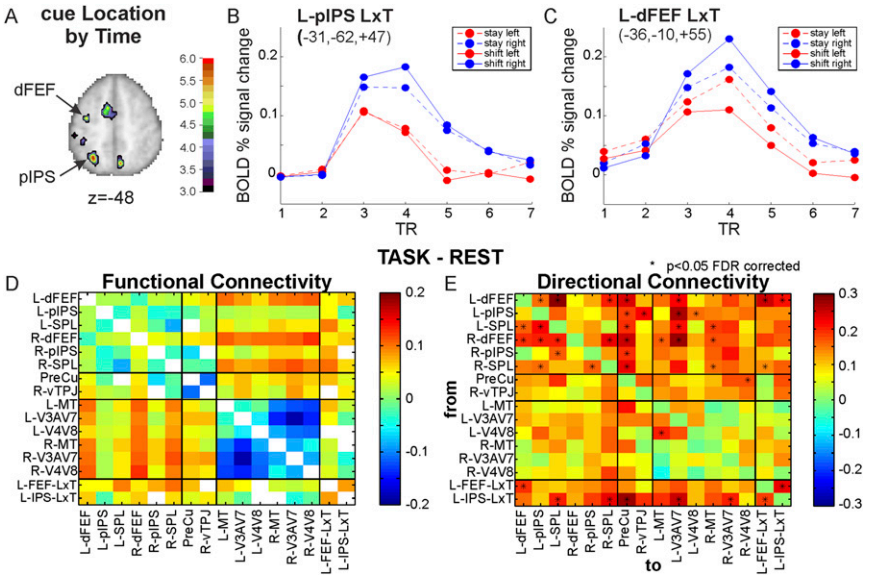

Fig. S2. DAN ROIs from LxT map. (*A*) One slice of the cue location by time map showing regions of the dorsal parietal cortex exhibiting a significant preference for cues presented in the contralateral hemifield. For the selected ROIs (L-IPS LxT and L-FEF LxT in *B* and *C*, respectively), we show time courses of the BOLD response to cue stimuli. Task-induced modulations of IFC and DFC for each ROI pair belonging to DAN, VIS, and DAN LxT are shown in *D* and *E*. The significant differences between rest and task conditions are evaluated by paired two-sample *t* tests; the pairs that do not significantly change their IFC are represented in white, whereas those that significantly change their DFC are indicated with an asterisk ($P = 0.05$, FDR corrected).

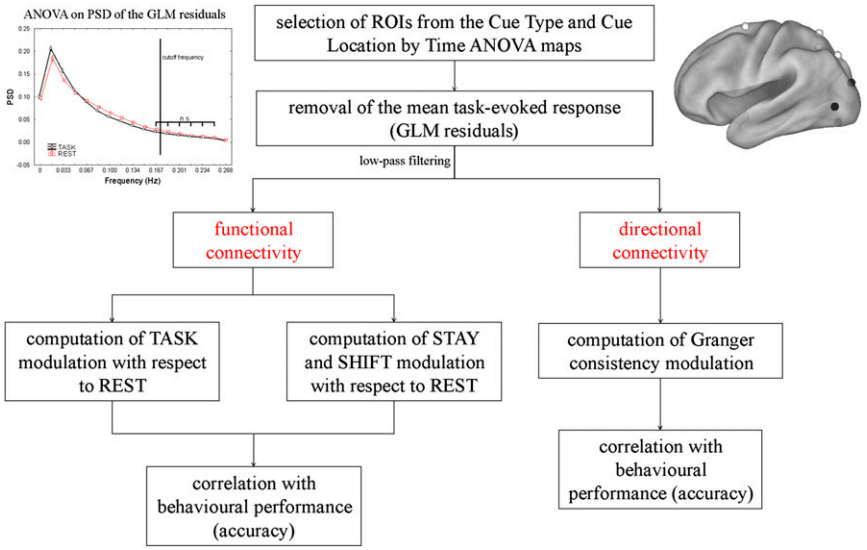

Fig. S3. Flowchart of the analysis method.

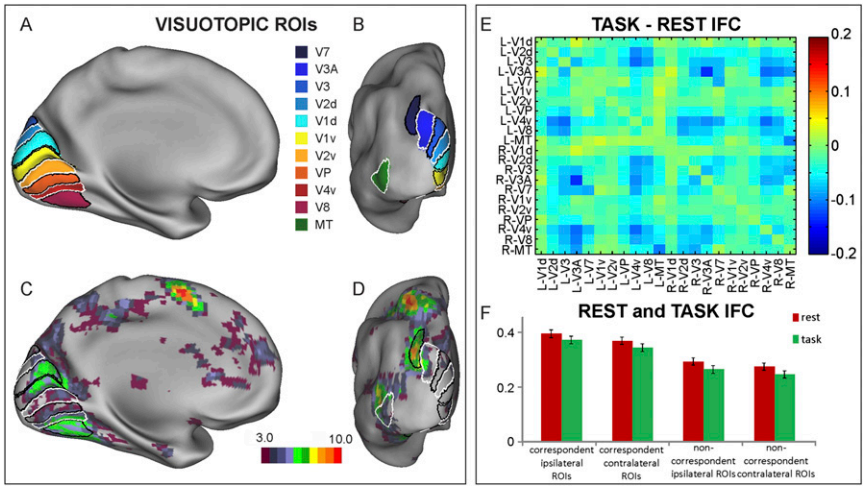

Fig. S4. Visuotopic ROIs selection and IFC results. Visuotopic regions represented on the inflated (*A*) medial and (*B*) posterior views of the left hemisphere. (*C* and *D*) Borders of visuotopic regions are overlaid on the voxels, showing a main effect of time in the voxelwise ANOVA with cue type, cue location, and time as factors, and from the intersection, the visuotopic ROIs were extracted. (*E*) Task-induced modulation of IFC within all of the extracted visuotopic ROIs and (*F*) bar plot of IFC during rest and task execution of early visual regions (V1–V2–V3/VP) averaged across correspondent/noncorrespondent ipsilateral/contralateral ROIs.

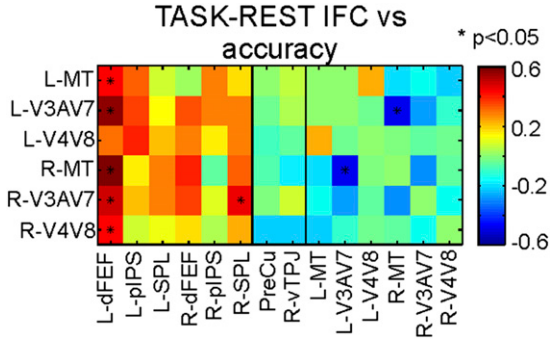

Fig. S5. Correlation between discrimination accuracy and IFC changes between task and rest. pIPS, posterior IPS.

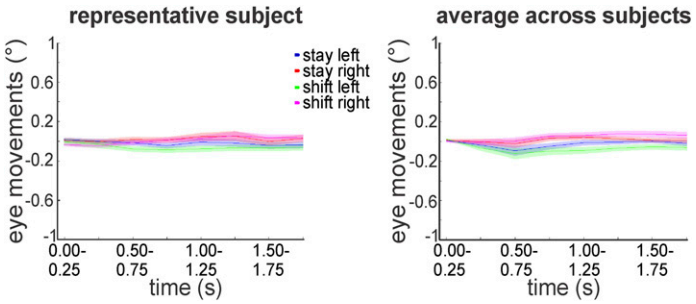

Fig. S6. Eye movements along the horizontal axis for one representative subject and the average across subjects.